Journal of the Brazilian Society of Mechanical Sciences and Engineering (2019) 41:49
https://doi.org/10.1007/s40430-018-1556-z

TECHNICAL PAPER

Numerical simulation of multiple steady and unsteady flow modes in a medium-gap spherical Couette flow

Suhail Abbas[1,2,3] · Li Yuan[2,3] · Abdullah Shah[4]

Received: 5 May 2018 / Accepted: 25 December 2018

Abstract

We study the multiple steady and unsteady flow modes in a medium-gap spherical Couette flow (SCF) by solving the three-dimensional incompressible Navier–Stokes equations. We have used an artificial compressibility method with an implicit line Gauss–Seidel scheme. The simulations are performed in SCF with only the inner sphere rotating. A medium-gap clearance ratio, $\sigma = \left(R_2 - R_1\right)/R_1 = 0.25$, has been used to investigate various flow states in a range of Reynolds numbers, $Re \in [400, 6500]$. First, we compute the 0-vortex basic flow directly from the Stokes flow as an initial condition. This flow exists up to $Re = 4900$ after which it evolves into spiral 0-vortex flows with wavenumber $s_p = 3, 4$ in the range $Re \in [4900, 6000]$, and then the flows become turbulent when $Re > 6000$. Second, we obtain the steady 1-vortex flow by using the 1-vortex flow at $Re = 700$ for $\sigma = 0.18$ as the initial conditions and found that it exists for $Re \in [480, 4300]$. The 1-vortex flow becomes wavy 1-vortex in the range $Re \in [4400, 5000]$. Further increasing the Reynolds number, we obtain new spiral waves of wavenumber $s_p = 3$ for $Re \in [5000, 6000]$. The flow becomes turbulent when $Re > 6000$. Third, we obtain the steady 2-vortex flow by using the 2-vortex flow at $Re = 900$ for $\sigma = 0.18$ as the initial conditions and found that it exists for $Re \in [700, 1900]$. With increasing Reynolds number the 2-vortex flow becomes partially wavy 2-vortex in the small range $Re \in [1900, 2100]$. We obtain distorted spiral wavy 2-vortex in the range $Re \in [4000, 5000]$. when $Re > 6000$ the flow evolves into spiral 0-vortex flow and becomes turbulent. The present flow scenarios with increasing Re agree well with the experimental results and further we obtain new flow states for the 1-vortex and 2-vortex flows.

Keywords Incompressible Navier–Stokes equation · WENO scheme · Line Gauss–Seidel scheme · Spherical Couette flow · Spiral wavy Taylor vortex

List of symbols

J	Determinant of coordinate transformation Jacobian
p	Pressure
n	Physical time level
m	Pseudo-time level
$\mathbf{I}$	Identity matrix
R_1	Radius of inner sphere
R_2	Radius of outer sphere
r, θ, ϕ	Spherical coordinates
l	Gauss–Seidel sweeps
$Re = \Omega R_1^2/\nu$	Reynolds number
Re_c	Critical Reynolds number
t	Physical time
U, V, W	Contra-variant velocity components
β	Artificial compressibility factor
$\sigma = \left(R_2 - R_1\right)/R_1$	Clearance ratio
ν	Kinematic viscosity
τ	Pseudo-time
ω_ϕ	Azimuthal vorticity component
Ω	Angular velocity
s_p	Spiral waves

Technical Editor: Jader Barbosa Jr., Ph.D.

✉ Suhail Abbas
suhailkiu156@gmail.com

1 Department of Mathematical Sciences, Karakorum International University, Gilgit, Pakistan

2 LSEC, Institute of Computational Mathematics and Scientific/Engineering Computing, Academy of Mathematics and Systems Science, Chinese Academy of Sciences, Beijing 100190, People's Republic of China

3 School of Mathematical Sciences, University of Chinese Academy of Sciences, Beijing 100190, People's Republic of China

4 Department of Mathematics, COMSATS University, Islamabad, Pakistan

1 Introduction

In many engineering applications such as hydraulic machinery and ship industry, numerical solution of the three-dimensional (3D) incompressible Navier–Stokes equations is required. A key issue in numerical solution of the incompressible Navier–Stokes equations is how to satisfy the continuity equation. In the past, two kinds of methods have been commonly used for incompressible flow simulations: The first kind is based on fractional step method [1–7] and the second is on artificial compressibility method [8, 9]. The fractional step method needs to solve the Poisson equation for pressure/pressure correction, which becomes complicated in 3D curvilinear grids [10]. The artificial compressibility method [2, 8, 9] avoids to solve the pressure Poisson equation. Rather, it introduces a pseudo-time derivative of the pressure term into the continuity equation so that the elliptic–parabolic type governing equations are transformed into the hyperbolic–parabolic type. The continuity equation is satisfied (approximately) when the pseudo-time derivative is marched toward zero (small tolerance in real computation). The main advantage of the artificial compressibility method is that it can reuse a large number of numerical techniques originally developed for compressible flow simulations. The disadvantage is that the convergence rate of the continuity equation may be slow and dependent on the artificial compressibility factor.

In the development of the artificial compressibility method, many investigators have used different upwind schemes to discretize the convective terms, e.g., flux difference splitting, MUSCL, WENO and DG schemes [7, 10–16]. To solve the discretized algebraic equations efficiently, many established algorithms like Beam-Warming approximate factorization schemes [17, 18], lower–upper symmetric Gauss–Seidel (LU-SGS) schemes [15, 19], point and line relaxation schemes [10, 20, 21], as well as GMRES and multigrid methods [10, 20, 21] were employed. In most cases, implicit algorithms were preferred due to their superior efficiency.

In this study, we use the line Gauss–Seidel (LGS) relaxation method [9, 21] along with a fifth-order finite difference WENO scheme [14, 15] for solving the artificial compressibility form of 3D incompressible Navier–Stokes equations in a generalized curvilinear coordinate system. We simulate different flow states in the spherical Couette flow (SCF) between two concentric spheres with the inner sphere rotating and the outer one fixed. The spherical gap is filled with a Newtonian fluid. This flow has two control parameters: a Reynolds number $\mathrm{Re} = \Omega R_1^2/\nu$, and a clearance ratio $\sigma = \left(R_2 - R_1\right)/R_1$, where Ω is the angular velocity of the inner sphere, ν is the kinematic viscosity of the fluid, and R_1, R_2 are the radii of the inner and outer spheres, respectively. The two control parameters, plus the initial conditions, completely determine the flow regimes consisting of different types of disturbances (e.g., different number of Taylor vortices, spiral waves, ring vortices). Owing to the simple geometry and the diversity of instabilities, SCF is an ideal template for studying the laminar-turbulent transition.

We simulate different flow states and transitions of SCF with increasing Reynolds number for a case of $\sigma = 0.25$ in the medium gap regime ($0.13 < \sigma <\approx 0.30$ [22]). Although many researchers have studied medium-gap clearance ratios [23–35], but there is only one experimental study [28] for $\sigma = 0.25$. The authors [28] obtained steady 1-vortex flow by counter-rotating the outer sphere for a short time in the range $420 \le Re \le 4200$. With increasing Reynolds number the flow becomes wavy at $Re \approx 4350$, and this wavy 1-vortex flow exists only to $Re \approx 4700$, after that the flow becomes turbulent. They obtained steady 2-vortex flow in the same way in the range $900 \le Re \le 1000$. With increasing Reynolds number the flow becomes spiral at $Re \approx 2000$. They also obtained spiral 0-vortex flow at higher Reynolds numbers from the 0-vortex basic flow that exists in the range $0 < Re \le 3800$. A summary of different flow modes was given in figure 6 in Ref. [28].

We investigate the flow modes in the wider range $Re \in [400, 6500]$ for $\sigma = 0.25$. We obtain steady 1- and 2-vortex flows, wavy 1-vortex flow and partially wavy 2-vortex flow, and spiral 0-, 1-, and 2-vortex flows in respective ranges of the Reynolds number, which basically agree with figure 6 in Ref. [28] and we further obtain new flow modes and transition paths.

The paper is organized as follows. In Sect. 2, we describe the governing equations and numerical methods. Section 3 represents the computational setup. Section 4 describes the numerical results and discussions of different flow modes and Sect. 5 concludes this paper.

2 Governing equations and numerical methods

2.1 Governing equations

We consider the artificial compressibility form of the incompressible 3D Navier–Stokes equations. In a fixed orthogonal generalized curvilinear coordinate system (ξ, η, ζ), the equations can be written in a strong conservative form [10],

$$\frac{\partial \hat{\mathbf{Q}}}{\partial \tau} + \mathbf{I}_m \frac{\partial \hat{\mathbf{Q}}}{\partial t} + \frac{\partial\left(\hat{\mathbf{E}} - \hat{\mathbf{E}}_v\right)}{\partial \xi} + \frac{\partial\left(\hat{\mathbf{F}} - \hat{\mathbf{F}}_v\right)}{\partial \eta} + \frac{\partial\left(\hat{\mathbf{G}} - \hat{\mathbf{G}}_v\right)}{\partial \zeta} = \mathbf{0}, \tag{1}$$

$$
\mathbf{I}_m = \mathrm{diag}(0,1,1,1), \quad \hat{\mathbf{Q}} = \frac{\mathbf{Q}}{J} = \frac{1}{J}\begin{bmatrix} p \\ u \\ v \\ w \end{bmatrix}, \quad \hat{\mathbf{E}} = \frac{1}{J}\begin{bmatrix} \beta U \\ Uu + \xi_x p \\ Uv + \xi_y p \\ Uw + \xi_z p \end{bmatrix},
$$

$$
\hat{\mathbf{F}} = \frac{1}{J}\begin{bmatrix} \beta V \\ Vu + \eta_x p \\ Vv + \eta_y p \\ Vw + \eta_z p \end{bmatrix}, \quad \hat{\mathbf{G}} = \frac{1}{J}\begin{bmatrix} \beta W \\ Wu + \zeta_x p \\ Wv + \zeta_y p \\ Ww + \zeta_z p \end{bmatrix}, \quad \hat{\mathbf{E}}_v = \frac{1}{\mathrm{Re}J}(\nabla\xi \cdot \nabla\xi)\mathbf{I}_m \frac{\partial \mathbf{Q}}{\partial \xi}, \tag{2}
$$

$$
\hat{\mathbf{F}}_v = \frac{1}{\mathrm{Re}J}(\nabla\eta \cdot \nabla\eta)\mathbf{I}_m \frac{\partial \mathbf{Q}}{\partial \eta}, \quad \hat{\mathbf{G}}_v = \frac{1}{\mathrm{Re}J}(\nabla\zeta \cdot \nabla\zeta)\mathbf{I}_m \frac{\partial \mathbf{Q}}{\partial \zeta},
$$

$$
U = \xi_x u + \xi_y v + \xi_z w, \quad V = \eta_x u + \eta_y v + \eta_z w, \quad W = \zeta_x u + \zeta_y v + \zeta_z w.
$$

Here, u, v, w are Cartesian velocity components, p is the pressure, $\mathbf{Q} = (p, u, v, w)$ is the solution vector, t is the physical time, τ is the pseudo-time, β is the artificial compressibility factor, U, V and W are the contra-variant velocity components in the ξ, η and ζ directions respectively. ξ_x, ξ_y, ξ_z etc are metric terms and J is the Jacobian of coordinate transformation.

2.2 Numerical methods

For spatial discretizations of Eq. (1), we apply a version of the fifth-order finite difference weighted non-oscillatory (WENO) scheme [14, 15] for the convective terms and a second-order central finite difference scheme for the viscous terms. For temporal discretizations, an implicit backward finite difference scheme is used for the pseudo-time derivative and a second-order, three-point backward difference scheme is used for the physical time derivatives, which give

$$
\frac{\mathbf{Q}^{n+1,m+1} - \mathbf{Q}^{n+1,m}}{J\Delta\tau} + \mathbf{I}_m \frac{1.5\mathbf{Q}^{n+1,m+1} - 2\mathbf{Q}^n + 0.5\mathbf{Q}^{n-1}}{J\Delta t} + \left[\frac{\partial\left(\hat{\mathbf{E}} - \hat{\mathbf{E}}_v\right)}{\partial\xi} + \frac{\partial\left(\hat{\mathbf{F}} - \hat{\mathbf{F}}_v\right)}{\partial\eta} + \frac{\partial\left(\hat{\mathbf{G}} - \hat{\mathbf{G}}_v\right)}{\partial\zeta} \right]^{n+1,m+1} = \mathbf{0}, \tag{3}
$$

where n is the physical time level and m is the pseudo-time level. We linearize the terms at $(m+1)$th level with respect to the mth level by using Taylor series expansion,

$$
\hat{\mathbf{E}}^{m+1} \approx \hat{\mathbf{E}}^m + \left(\frac{\partial \hat{\mathbf{E}}}{\partial \mathbf{Q}}\right)^m \left(\mathbf{Q}^{m+1} - \mathbf{Q}^m\right) = \hat{\mathbf{E}}^m + \mathbf{A}\Delta\mathbf{Q}^m, \tag{4}
$$

$$
\hat{\mathbf{E}}_v^{m+1} \approx \hat{\mathbf{E}}_v^m + \left(\frac{\partial \hat{\mathbf{E}}_v}{\partial \mathbf{Q}}\right)^m \left(\mathbf{Q}^{m+1} - \mathbf{Q}^m\right) = \hat{\mathbf{E}}_v^m + \mathbf{\Gamma}_1 \Delta\mathbf{Q}^m, \tag{5}
$$

where $\Delta\mathbf{Q}^m = \mathbf{Q}^{n+1,m+1} - \mathbf{Q}^{n+1,m}$, $\mathbf{A} = (\partial\hat{\mathbf{E}}/\partial\mathbf{Q})^m$ is the Jacobian matrix of the convective flux vector, and $\mathbf{\Gamma}_1 = (\partial\hat{\mathbf{E}}_v/\partial\mathbf{Q})^m = \frac{1}{ReJ}(\nabla\xi \cdot \nabla\xi)\mathbf{I}_m \partial_\xi$ is the Jacobian matrix (operator) of the viscous flux vector. Similar linearizations are made for $\hat{\mathbf{F}}^{m+1}$, $\hat{\mathbf{F}}_v^{m+1}$, $\hat{\mathbf{G}}^{m+1}$ and $\hat{\mathbf{G}}_v^{m+1}$. The superscript $n+1$ on each variable in (4)–(5) has been suppressed for simple notation. Substituting (4)–(5) and similar expressions into (3), we obtain the delta form,

$$
\begin{aligned}
&\left\{ \frac{\mathbf{I}}{J\Delta\tau} + 1.5\frac{\mathbf{I}_m}{J\Delta t} + \left[\frac{\partial\left(\mathbf{A} - \mathbf{\Gamma}_1\right)}{\partial\xi} + \frac{\partial\left(\mathbf{B} - \mathbf{\Gamma}_2\right)}{\partial\eta} + \frac{\partial\left(\mathbf{C} - \mathbf{\Gamma}_3\right)}{\partial\zeta} \right] \right\} \Delta\mathbf{Q}^m = \\
&\quad - \left[\frac{\partial\left(\hat{\mathbf{E}} - \hat{\mathbf{E}}_v\right)}{\partial\xi} + \frac{\partial\left(\hat{\mathbf{F}} - \hat{\mathbf{F}}_v\right)}{\partial\eta} + \frac{\partial\left(\hat{\mathbf{G}} - \hat{\mathbf{G}}_v\right)}{\partial\zeta} \right]^m - \frac{\mathbf{I}_m}{J\Delta t}\left(1.5\mathbf{Q}^m - 2\mathbf{Q}^n + 0.5\mathbf{Q}^{n-1}\right) \\
&\quad \equiv \mathbf{R}^m,
\end{aligned} \tag{6}
$$

where $\mathbf{I}$ is the identity matrix.

The Jacobian matrices $\mathbf{A} = \partial\hat{\mathbf{E}}/\partial\mathbf{Q}, \mathbf{B} = \partial\hat{\mathbf{F}}/\partial\mathbf{Q}$ and $\mathbf{C} = \partial\hat{\mathbf{G}}/\partial\mathbf{Q}$ can be computed as

$$
\mathbf{A}_i = \frac{1}{J}\begin{bmatrix} 0 & k_x\beta & k_y\beta & k_z\beta \\ k_x & k_x u + \Theta & k_y u & k_z u \\ k_y & k_x v & k_y v + \Theta & k_z v \\ k_z & k_x w & k_y w & k_z w + \Theta, \end{bmatrix}, \tag{7}
$$

where $\mathbf{A}_i = \mathbf{A},\ \mathbf{B},\ \mathbf{C}$ for $i = 1, 2, 3$ respectively, and $\Theta = k_x u + k_y v + k_z w$, $k_x = \frac{\partial \xi_i}{\partial x}$, $k_y = \frac{\partial \xi_i}{\partial y}$, $k_z = \frac{\partial \xi_i}{\partial z}$, with $\xi_i = \xi, \eta, \zeta$ for $i = 1, 2, 3$, respectively.

The matrices $\mathbf{A}, \mathbf{B}, \mathbf{C}$ can be diagonalized by using the similarity transformation

$$\mathbf{A}_i = \mathbf{T}_i \Lambda_i \mathbf{T}_i^{-1} \tag{8}$$

so that

$$\mathbf{A}_i^{\pm} = \mathbf{T}_i \boldsymbol{\Lambda}_i^{\pm} \mathbf{T}_i^{-1}, \tag{9}$$

where $\boldsymbol{\Lambda}_i^{\pm} = \frac{1}{2}\left(\boldsymbol{\Lambda}_i \pm |\boldsymbol{\Lambda}_i|\right)$ is a diagonal matrix. Further details can be found in [7, 21, 36].

To reduce the bandwidth of the discretized matrix equations, the convective terms in the LHS of Eq. (6) are approximated with the first-order upwind scheme and the viscous terms in the LHS are approximated with the traditional central difference. The convective terms in the RHS are still discretized with the fifth-order WENO scheme. The fully discretized equations can be written as

$$\begin{aligned}
&\left[\frac{1}{J}\left(\frac{\mathbf{I}}{\Delta\tau} + \frac{1.5\mathbf{I}_m}{\Delta t}\right) + \left(\mathbf{A}^+ + \boldsymbol{\Gamma}_1\right)_{i-\frac{1}{2}} - \left(\mathbf{A}^- - \boldsymbol{\Gamma}_1\right)_{i+\frac{1}{2}} + \left(\mathbf{B}^+ + \boldsymbol{\Gamma}_2\right)_{j-\frac{1}{2}}\right. \\
&\quad \left. -\left(\mathbf{B}^- - \boldsymbol{\Gamma}_2\right)_{j+1/2} + \left(\mathbf{C}^+ + \boldsymbol{\Gamma}_3\right)_{k-\frac{1}{2}} - \left(\mathbf{C}^- - \boldsymbol{\Gamma}_3\right)_{k+\frac{1}{2}}\right] \Delta\mathbf{Q}^m_{i,j,k} \\
&\quad - \left(\mathbf{A}^+ + \boldsymbol{\Gamma}_1\right)_{i-\frac{1}{2}} \Delta\mathbf{Q}^m_{i-1,j,k} + \left(\mathbf{A}^- - \boldsymbol{\Gamma}_1\right)_{i+\frac{1}{2}} \Delta\mathbf{Q}^m_{i+1,j,k} \\
&\quad - \left(\mathbf{B}^+ + \boldsymbol{\Gamma}_2\right)_{j-\frac{1}{2}} \Delta\mathbf{Q}^m_{i,j-1,k} + \left(\mathbf{B}^- - \boldsymbol{\Gamma}_2\right)_{j+\frac{1}{2}} \Delta\mathbf{Q}^m_{i,j+1,k} \\
&\quad - \left(\mathbf{C}^+ + \boldsymbol{\Gamma}_3\right)_{k-\frac{1}{2}} \Delta\mathbf{Q}^m_{i,j,k-1} + \left(\mathbf{C}^- - \boldsymbol{\Gamma}_3\right)_{k+\frac{1}{2}} \Delta\mathbf{Q}^m_{i,j,k+1} = \mathbf{R}^m,
\end{aligned} \tag{10}$$

which constitute a sparse seven diagonal linear system of equations. In this study, we use a line Gauss–Seidel scheme (LGS) to solve (10).

2.2.1 Line Gauss–Seidel scheme

We use the line Gauss–Seidel scheme as in Rogers and Kwak [8] and Yuan [21]. In this scheme, an implicit direction is chosen such that the LHS terms of Eq. (10) from points along a grid line in this direction are solved for simultaneously, while all other LHS terms from points off this grid line are multiplied by the most recently calculated $\Delta\mathbf{Q}$ and moved to the RHS. For example, if we take the ξ direction as the implicit direction while doing GS sweep in the $\eta - \zeta$ plane, then Eq. (10) is written as a block-tridiagonal system:

$$\begin{aligned}
&- \left(\mathbf{A}^+ + \boldsymbol{\Gamma}_1\right)_{i-\frac{1}{2}} \Delta\mathbf{Q}^m_{i-1,j,k} + \left[\frac{1}{J}\left(\frac{\mathbf{I}}{\Delta\tau} + \frac{1.5\mathbf{I}_m}{\Delta t}\right) + \left(\mathbf{A}^+ + \boldsymbol{\Gamma}_1\right)_{i-\frac{1}{2}} - \left(\mathbf{A}^- - \boldsymbol{\Gamma}_1\right)_{i+\frac{1}{2}}\right. \\
&\left. + \left(\mathbf{B}^+ + \boldsymbol{\Gamma}_2\right)_{j-\frac{1}{2}} - \left(\mathbf{B}^- - \boldsymbol{\Gamma}_2\right)_{j+\frac{1}{2}} + \left(\mathbf{C}^+ + \boldsymbol{\Gamma}_3\right)_{k-\frac{1}{2}} - \left(\mathbf{C}^- - \boldsymbol{\Gamma}_3\right)_{k+\frac{1}{2}}\right] \Delta\mathbf{Q}^m_{i,j,k} \\
&+ \left(\mathbf{A}^- - \boldsymbol{\Gamma}_1\right)_{i+\frac{1}{2}} \Delta\mathbf{Q}^m_{i+1,j,k} \\
&= \mathbf{R}^m + \left(\mathbf{B}^+ + \boldsymbol{\Gamma}_2\right)_{j-\frac{1}{2}} \Delta\mathbf{Q}^m_{i,j-1,k} - \left(\mathbf{B}^- - \boldsymbol{\Gamma}_2\right)_{j+\frac{1}{2}} \Delta\mathbf{Q}^m_{i,j+1,k} \\
&\qquad + \left(\mathbf{C}^+ + \boldsymbol{\Gamma}_3\right)_{k-\frac{1}{2}} \Delta\mathbf{Q}^m_{i,j,k-1} - \left(\mathbf{C}^- - \boldsymbol{\Gamma}_3\right)_{k+\frac{1}{2}} \Delta\mathbf{Q}^m_{i,j,k+1}.
\end{aligned} \tag{11}$$

We solve Eq. (11) by using a block tridiagonal solver for all $\Delta\mathbf{Q}^m_{i,j,k}$ along a ξ-grid line at indices (j, k), and update the solution at $(m+1)$th level using $\mathbf{Q}^{n+1,m+1}_{i,j,k} = \mathbf{Q}^{n+1,m}_{i,j,k} + \Delta\mathbf{Q}^{m,(l)}_{i,j,k}$ as well as $\mathbf{A}$,$\mathbf{B}$, $\mathbf{C}$, $\mathbf{R}^m$ after l GS sweeps (a forward and backward sweep counts one GS sweep) in the η-ζ plane. We set $\Delta\mathbf{Q}^{m,(0)} = 0$ as initialization for the sweep. The boundary conditions are treated implicitly. After some experiments we find that $l = 1$ is optimal for unsteady computations. The forward or backward sweep is parallelized with a pipeline method using OpenMP.

3 Computational setup

The computational domain of the spherical gap is divided into a number of grid points along the radial (r), meridional (θ) and azimuthal (ϕ) directions, respectively. The grid points are clustered near the walls along the r direction and are uniform along the θ and ϕ directions as shown in Fig. 1. The grid point number used is $41(r) \times 361(\theta) \times 153(\phi)$.

The no-slip boundary conditions are applied to the velocities on the inner and outer spheres. The pressure on the walls is obtained from the radial component of the momentum equations written in the spherical coordinate system, and the numerical polar boundary is treated by letting the flow variables on the polar axis equal to averages of the grid points next to the polar axis. A reference pressure is taken at a fixed interior point of the computational domain and the solved pressure at each grid point is subtracted by this value.

The non-dimensional physical time step $\Delta t = 0.025$ and Newton iteration for the pseudo-time marching are used. The sub-iteration (pseudo-time marching) is carried out

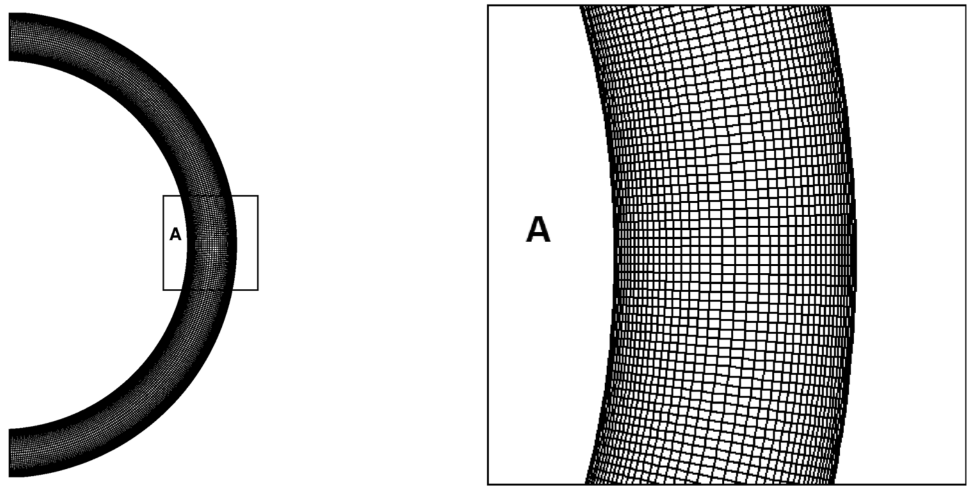

Fig. 1 Computational mesh for clearance ratio $\sigma = 0.25$ in a meridional plane (left) and a close view of zone **A** (right)

until the L_2-norm of the residual $\mathbf{R}^m$ is reduced by 2–3 orders of magnitude or a maximum iteration number is reached. An artificial compressibility factor $\beta = 1$ has been used.

4 Numerical results and discussions

For the clearance ratio $\sigma = 0.25$, figure 6 of Ref. [28] gave existence regimes and critical Reynolds numbers for different kinds of flow modes including Taylor vortices, disturbed Taylor vortices, wavy Taylor vortices, spiral Taylor vortices, and spiral waves. Based on that figure, we study the range $Re \in [400, 6500]$ to cover all the flow modes mentioned above. To resolve critical Reynolds numbers, we use a step of $\Delta Re = 10$. The present numerical results are compared with the experimental results [28]. Newly found flow disturbances are described in Sects. 4.2 and 4.3.

4.1 Taylor vortex flow

First, we compute the 0-vortex flow at $Re = 400$ directly by using Stokes flow as the initial conditions. Then with increments of $\Delta Re = 100$ and $\Delta Re = 10$, we have found that the 0-vortex flow can exist from very small Re up to $Re = 4900$. Figure 2 shows computed contours of meridional streamlines, angular velocity $u_\phi / r\sin(\theta)$ and azimuthal vorticity ω_ϕ for the 0-vortex flow at $Re = 700$.

The critical Reynolds number Re_c for the occurrence of the 1-vortex flow is a function of the clearance ratio

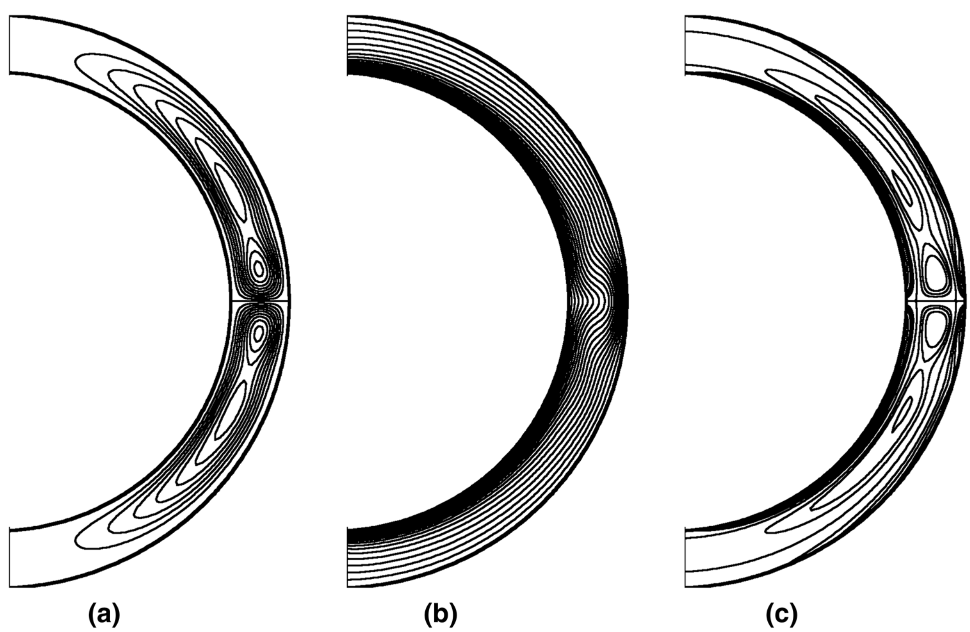

Fig. 2 Steady 0-vortex flow for $\beta = 0.25$ at $Re = 700$. **a** streamlines; **b** angular velocity $u_\phi / r\sin(\theta)$; **c** azimuthal vorticity ω_ϕ

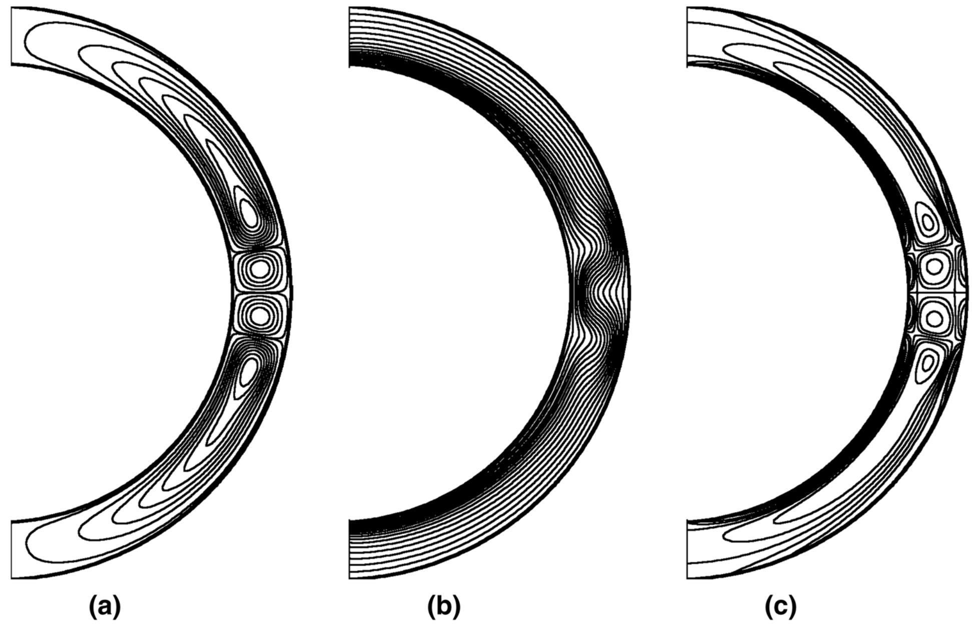

Fig. 3 Steady 1-vortex flow for $\beta = 0.25$ at $Re = 700$, **a** streamlines; **b** angular velocity $u_\phi / r \sin(\theta)$; **c** azimuthal vorticity ω_ϕ

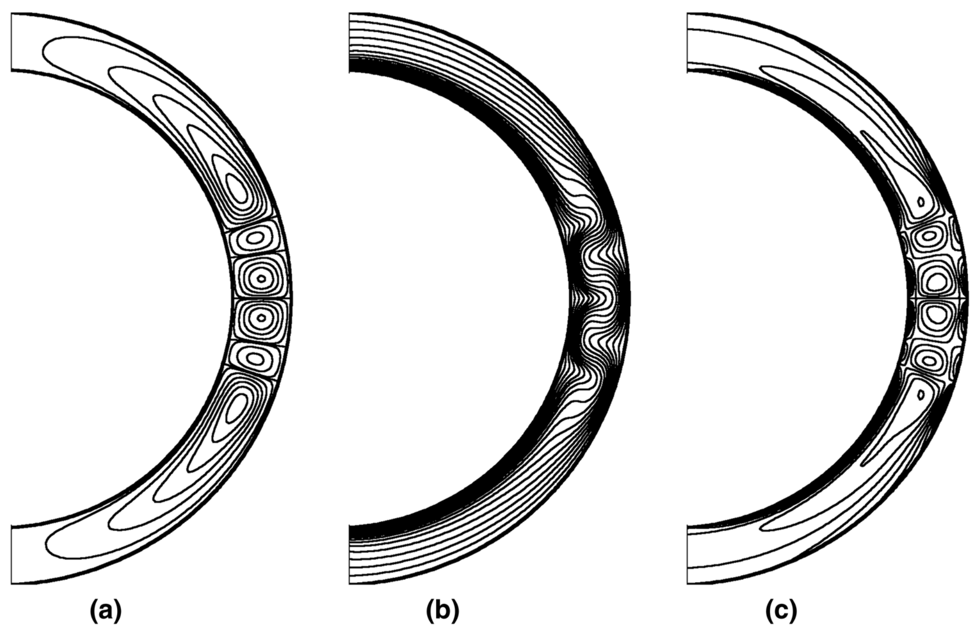

Fig. 4 Steady 2-vortex flow for $\beta = 0.25$ at $Re = 700$, **a** streamlines; **b** angular velocity $u_\phi / r \sin(\theta)$; **c** azimuthal vorticity ω_ϕ

σ. Yavorskaya et al. [23] found an empirical formula $Re_c = 41.3(1+\sigma)\sigma^{-3/2}$ for the range $0.08 \le \sigma \le 0.25$ and an experimental fit for the maximum number i of Taylor vortex pairs as $i = 0.21\sigma^{-4/3}$. For $\sigma = 0.25$ the two formulas give $\mathrm{Re}_c = 413$ and $i = 1.33$. According to previous studies and our own trial, it is not possible to obtain the 1-vortex flow from the Stokes flow initial conditions. We obtain the 1-vortex flow by using the 1-vortex flow for $\sigma = 0.18$ at $Re = 700$ as the initial conditions and increasing σ suddenly from 0.18 to 0.25 [37, 38]. The computed streamlines, angular velocity $u_\phi / r \sin(\theta)$ and azimuthal vorticity ω_ϕ for the steady 1-vortex flow at $Re = 700$ are shown in Fig. 3. By increasing and decreasing the Reynolds number with $\Delta Re = 100$ and 10, we have determined $\mathrm{Re}_c = 480$ and the existence of the steady 1-vortex flow is $480 \le Re \le 4300$, close to the experimental regime $420 \le Re \le 4200$ [28].

Similarly, we can obtain the steady 2-vortex flow [39, 40] for $\sigma = 0.25$ by using the 2-vortex flow for $\sigma = 0.18$ at $Re = 900$ as the initial conditions and increasing σ from 0.18 to 0.25 suddenly. We find this flow exists in the range of $700 \le Re \le 1900$, which is larger than the experimental range $900 \le Re \le 1000$ of Junk and Egbers [28].

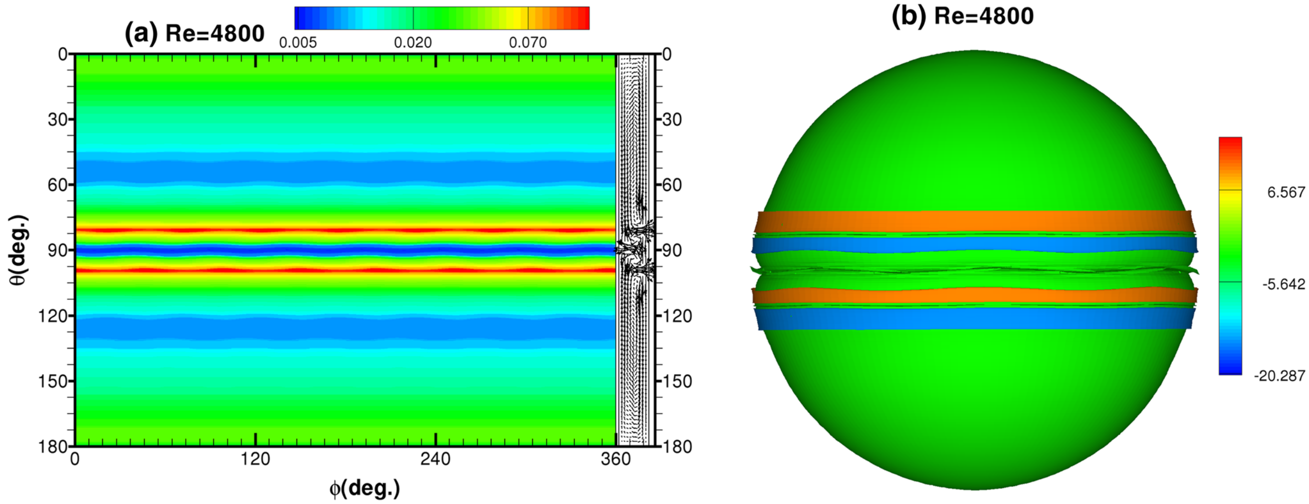

Fig. 5 Wavy 1-vortex flow with wavenumber $m = 7$ at $Re = 4800$, **a** flooded contours of the azimuthal angular velocity $\omega = v_\phi / r\sin(\theta)$ on the unwrapped middle spherical surface $r = 1 + 0.5\sigma$, $0 \le \theta \le \pi$, $0 \le \phi \le 2\pi$ on the left, and the right graph shows the meridional velocity vectors (v_r, v_θ) in the meridional plane $\phi = 2\pi$. **b** The front view of iso-surfaces of positive and negative azimuthal vorticity components of levels ±0.9

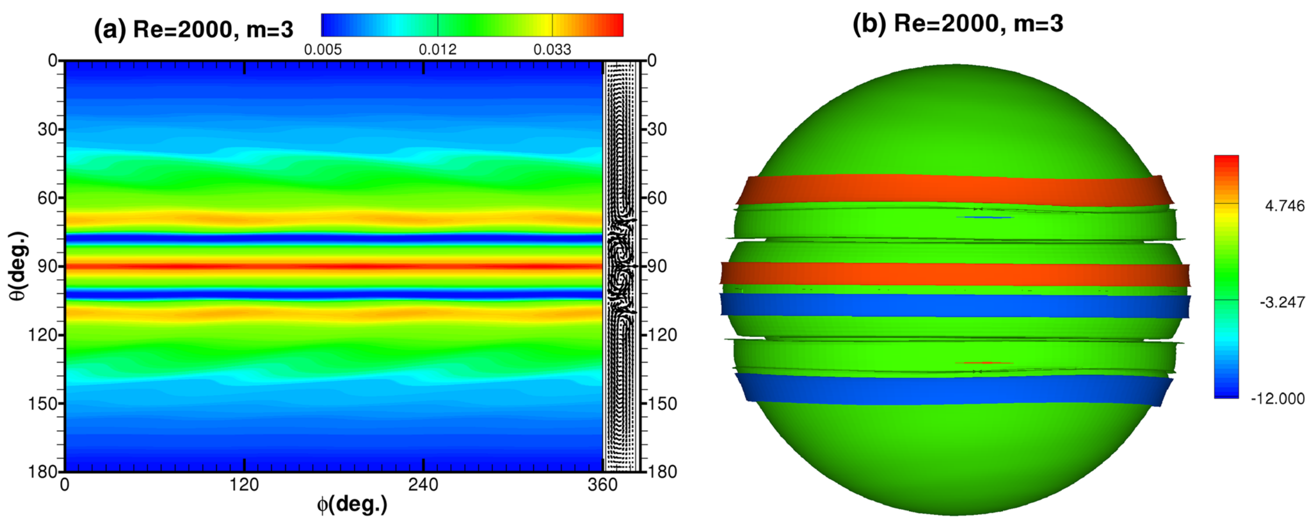

Fig. 6 Partially wavy 2-vortex flow with wavenumber $m = 3$ at $Re = 2000$. **a** Contours of the azimuthal angular velocity $\omega = v_\phi / r\sin(\theta)$ on the unwrapped middle spherical surface $r = 1 + 0.5\sigma$, $0 \le \theta \le \pi$, $0 \le \phi \le 2\pi$ on the left, and the right graph shows the meridional velocity vectors (v_r, v_θ) in the meridional plane $\phi = 2\pi$. **b** The front view of iso-surfaces of positive and negative azimuthal vorticity components of levels ±0.9

Figure 4 shows the computed streamlines, angular velocity $u_\phi / r\sin(\theta)$ and azimuthal vorticity ω_ϕ of the steady 2-vortex flow at $Re = 700$. It is remarked that the above three steady flows are axially and equatorially symmetric.

4.2 Wavy Taylor vortex flow

In order to obtain the wavy 1-vortex flow, we use the steady 1-vortex flow at $Re = 4300$ as the initial conditions, and increase the Reynolds number with increments of $\Delta Re = 100$ and 10. The flow becomes wavy Taylor vortex flow with $m = 7$ traveling waves imposed on the toroidal 1-pair of Taylor vortices at $Re_c \approx 4400$ that is slightly larger than $Re \approx 4350$ in the experiment [28]. This wavy 1-vortex flow remains up to $Re = 5000$, then it evolves into the spiral wavy flow to be described in Sect. 4.3 when $Re > 5000$. Figure 5 shows the wavy 1-vortex flow at $Re = 4800$.

Similarly, we obtain the wavy 2-vortex flow by using the steady 2-vortex flow at $Re = 1100$ as the initial conditions and increasing Re with steps of $\Delta Re = 100$ and 10. Up to

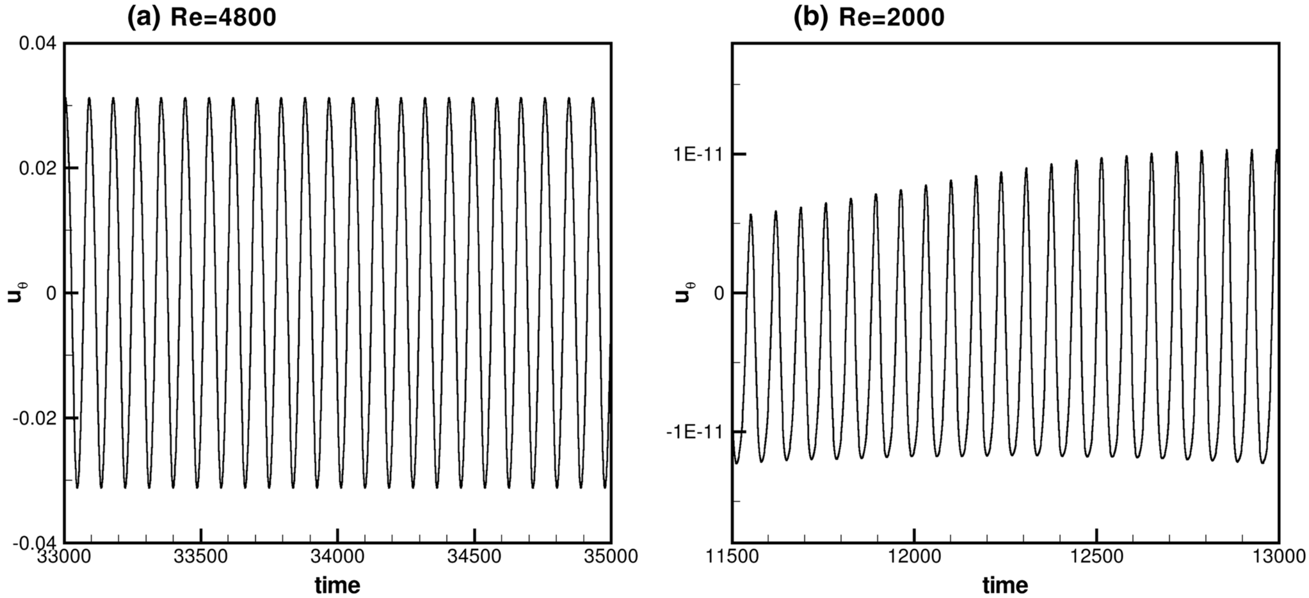

Fig. 7 Time history of the meridional velocity component u_θ at a point $(r, \theta, \phi) = (1 + \beta/2, \pi/2, 0)$: **a** wavy 1-vortex flow at $Re = 4800$; **b** wavy 2-vortex flow at $Re = 2000$

Fig. 8 North pole view of colored contours of the azimuthal vorticity component ω_ϕ of different spiral waves with zero vortex at four different Reynolds numbers. The inner sphere rotates counterclockwise

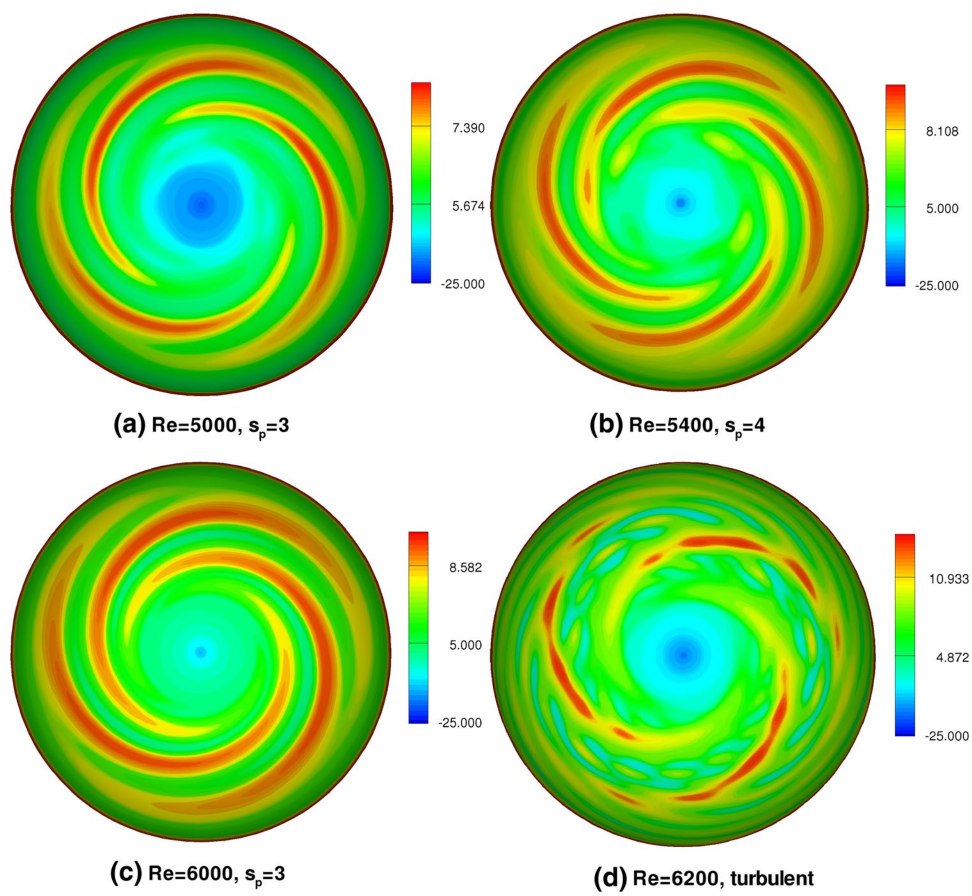

Re < 1900 we obtain stable 2-vortex flow. However, we obtain a *new* partially wavy 2-vortex flow with $m = 3$ traveling waves imposed on the outer one of the two vortices in the range of $Re \in [1900, 2100]$. Figure 6 shows the partially wavy 2-vortex flow at $Re = 2000$. The experimental results (figure 6 in Ref. [28]) shown that there is only "spiral Taylor vortices" at $Re = 2000$, but they did not give the existence range and the flow visualization. We have found that it is the partially wavy 2-vortex flow and this flow exists within the range of Reynolds number $Re \in [1900, 2100]$. After Re>2100 it again evolves into the 0-vortex basic flow, and this basic flow remains stable till we get some spirals at higher Reynolds number which we will explain in the next section.

Figure 7 shows the velocity-time series at a point $(r, \theta, \phi) = (1 + \beta/2, \pi/2, 0)$ for the wavy 1-vortex and wavy 2-vortex flows at $Re = 4800$ and $Re = 2000$, respectively. The fluctuations in the velocity-time series clearly show the wavy nature of the flow.

4.3 Spiral wavy flow

Spiral waves appear in high latitude regions in each hemisphere at high Reynolds numbers [41]. We can obtain spiral wavy flows by using the supercritical 0-vortex flow and wavy 1- and 2-vortex flows as the initial conditions.

First, we use the supercritical 0-vortex flow at $Re = 4900$ as the initial conditions and increasing the Reynolds number with $\Delta Re = 100$. We obtain spiral waves of wavenumber $s_p = 3$ with 0-vortex at $Re = 5000$ as shown in Fig. 8a. Further increasing the Reynolds number, we get spiral waves of wavenumber $s_p = 4$ at $Re = 5400$ as shown in Fig. 8b. Still further increasing the Reynolds number to 6000, the four spiral waves evolve into $s_p = 3$ spiral waves again as shown

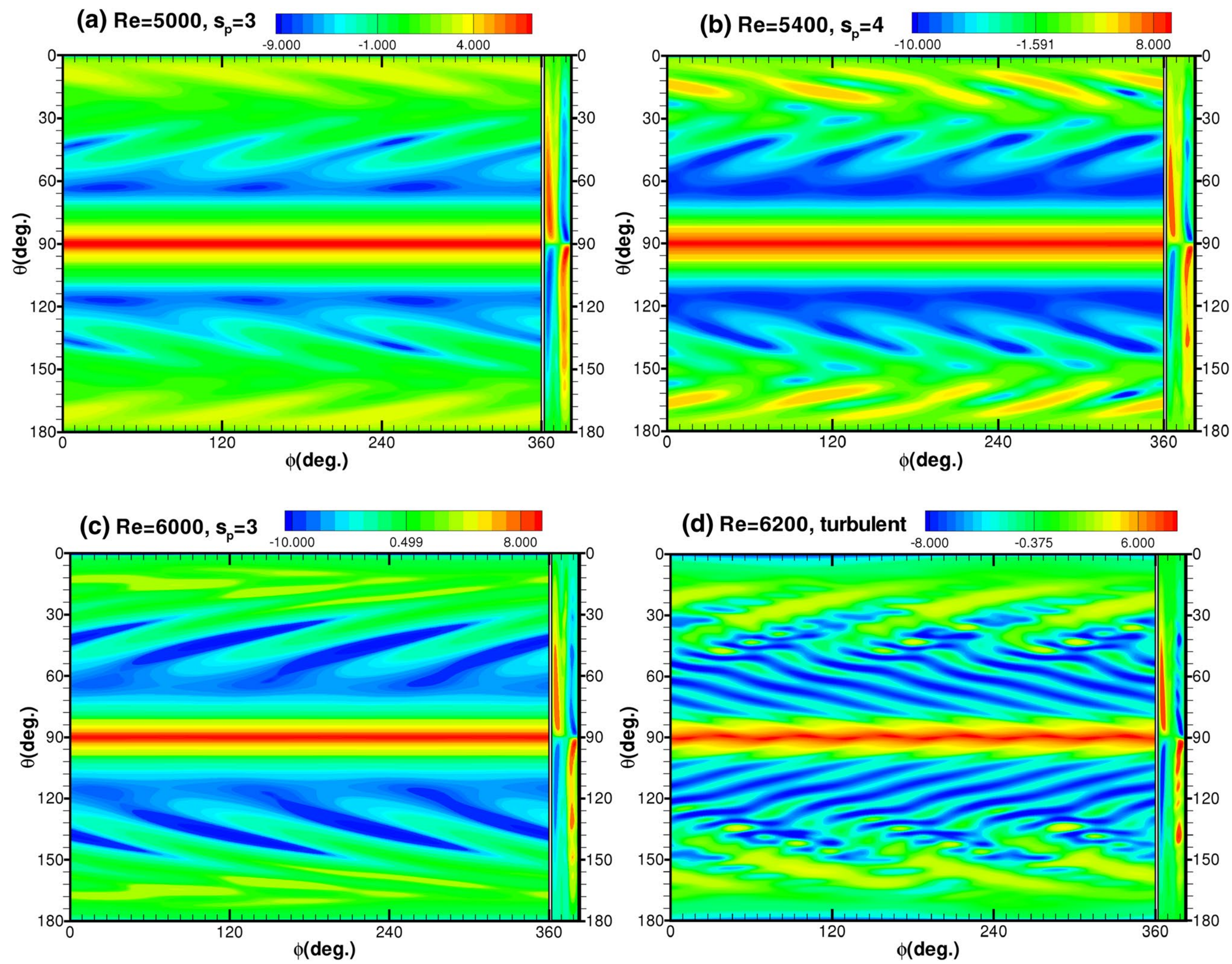

Fig. 9 Contours of the azimuthal angular velocity $\omega = v_\phi / r\sin(\theta)$ of spiral 0-vortex flow at four different Reynolds numbers on the unwrapped middle spherical surface $r = 1 + 0.5\sigma$, $0 \le \theta \le \pi$, $0 \le \phi \le 2\pi$ on the left graph for each subfigure, while the right narrow graph shows streamlines in the meridional plane at $\phi = 2\pi$. The flows are same as in Fig. 8

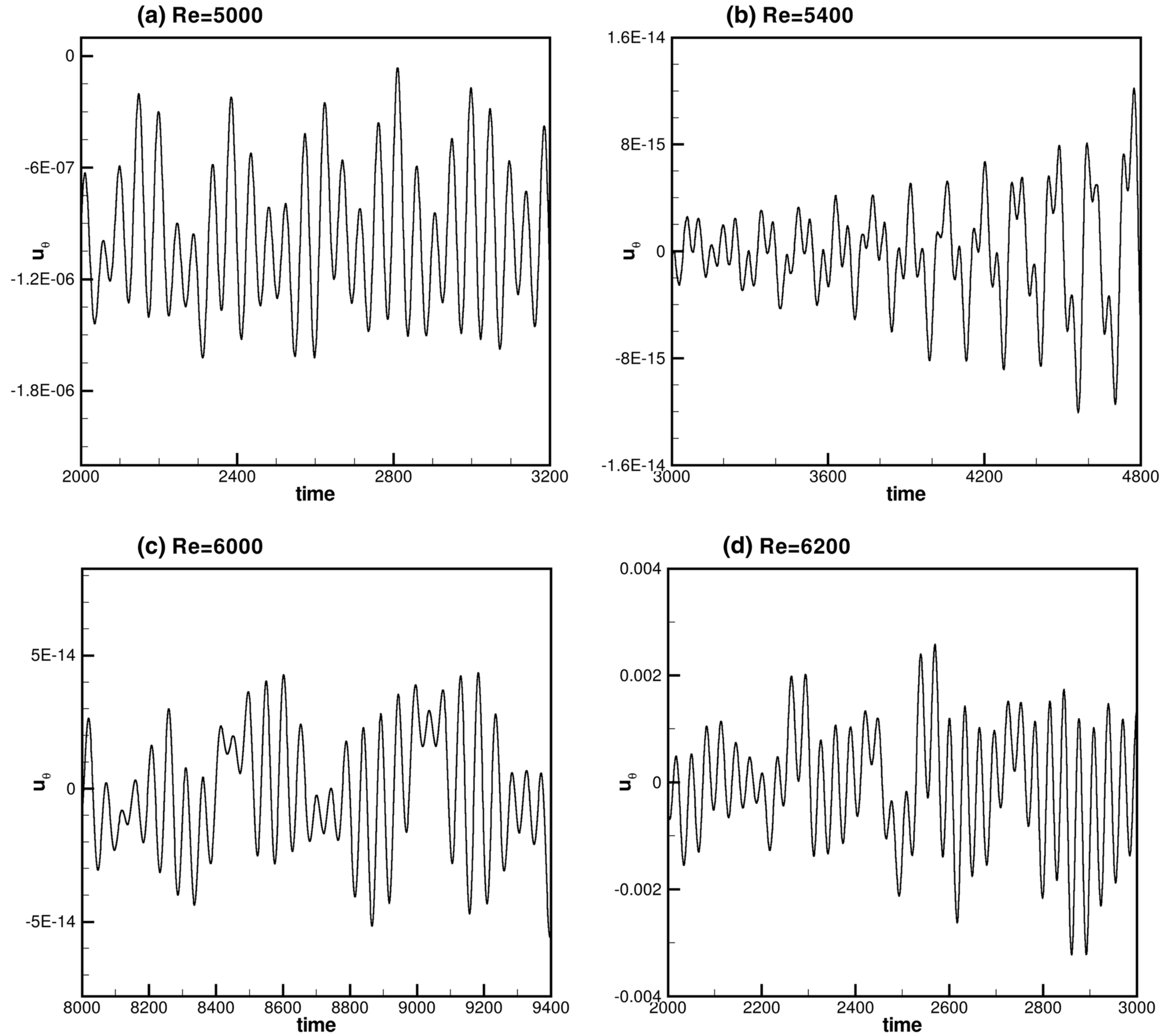

Fig. 10 Time history of the meridional velocity component u_θ of spiral wavy 0-vortex flow at a point $(r, \theta, \phi) = (1 + \beta/2, \pi/2, 0)$: **a** $Re = 5000$; **b** $Re = 5400$; **c** $Re = 6000$; and **d** $Re = 6200$

Fig. 11 North pole view of the colored contours of the azimuthal vorticity component ω_ϕ of spiral waves imposed on the 1-vortex flow at two different Reynolds numbers. The inner sphere is rotating counterclockwise

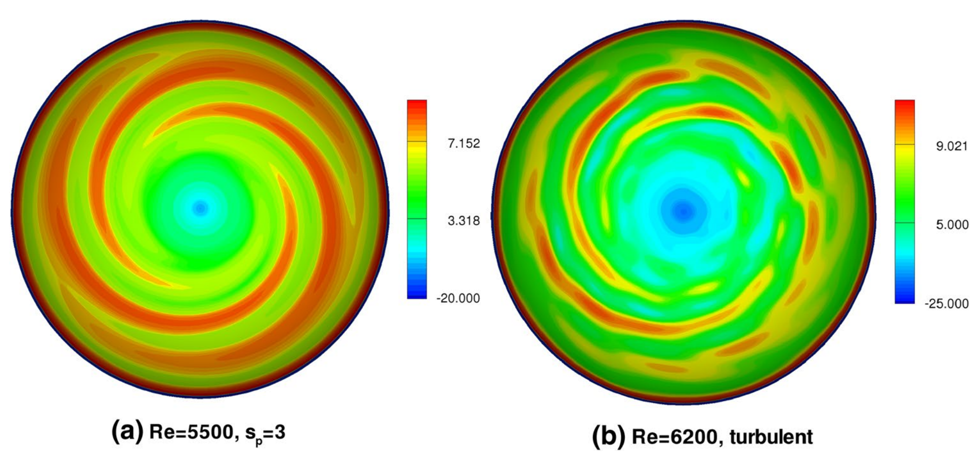

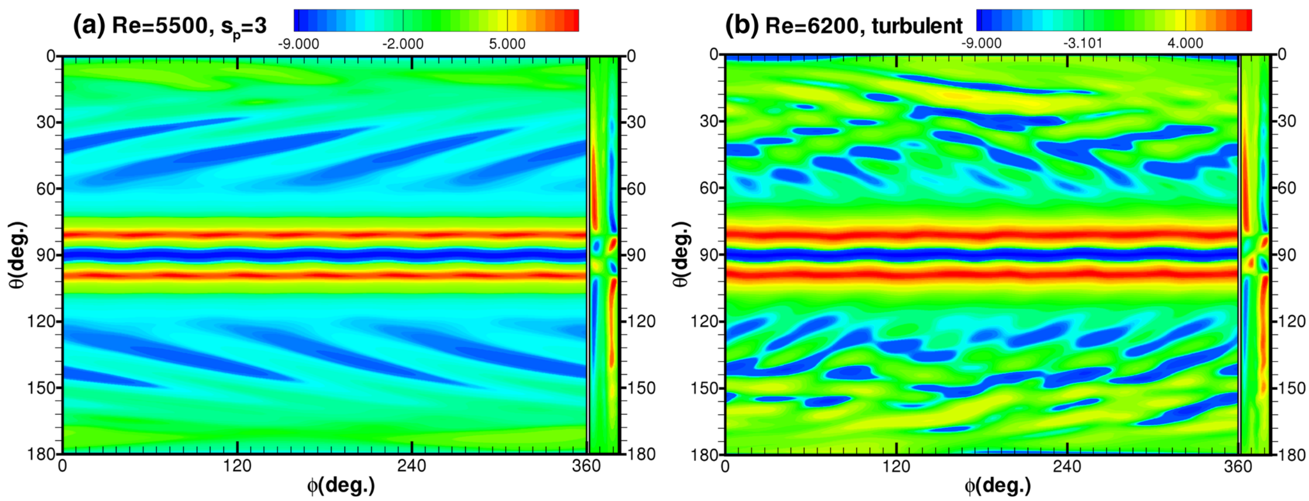

Fig. 12 Contours of the azimuthal angular velocity $\omega = v_\phi / r\sin(\theta)$ of the spiral wavy 1-vortex flow at different Reynolds numbers on the middle spherical surface $r = 1 + 0.5\sigma$, $0 \le \theta \le \pi$, $0 \le \phi \le 2\pi$ on the left frame for each figure, while the right graph shows the streamlines in the meridional plane at $\phi = 2\pi$

in Fig. 8c. The spiral flow becomes segmented and finally becomes turbulent when $Re \ge 6200$ as shown in Fig. 8d. It can be seen that the spiral waves have clockwise spirals extending from the high latitude to the equatorial regions. The inner sphere rotates in the counterclockwise direction.

Figure 9a–d shows the azimuthal angular velocity ($\omega = v_\phi / r\sin(\theta)$) in the (θ, ϕ)-plane in spherical surface $r = 1 + 0.5\sigma$, $0 \le \theta \le \pi$, $0 \le \phi \le 2\pi$ corresponding to Fig. 8. It can be observed that the spiral waves close to the equator have clockwise spirals from the middle latitude to the equatorial sides, while there are small spirals close to the pole which have counterclockwise spirals from the high latitude to low latitude regions. The outflow boundary at the equator of the zero vortex flow is parallel to the equator for $Re < 6000$. But for the turbulent case in Fig. 9d, the outflow boundary becomes wavy in the ϕ direction due to the penetration of the turbulent spiral zones towards the equator.

Figure 10 shows the velocity-time series at a point $(r, \theta, \phi) = (1 + \beta/2, \pi/2, 0)$ for the spiral wavy 0-vortex flow at $Re = 5000$, 5400, 6000 and 6200 respectively.

Second, we simulate the spiral wavy 1-vortex flow at higher Reynolds numbers by using the wavy 1-vortex flow at

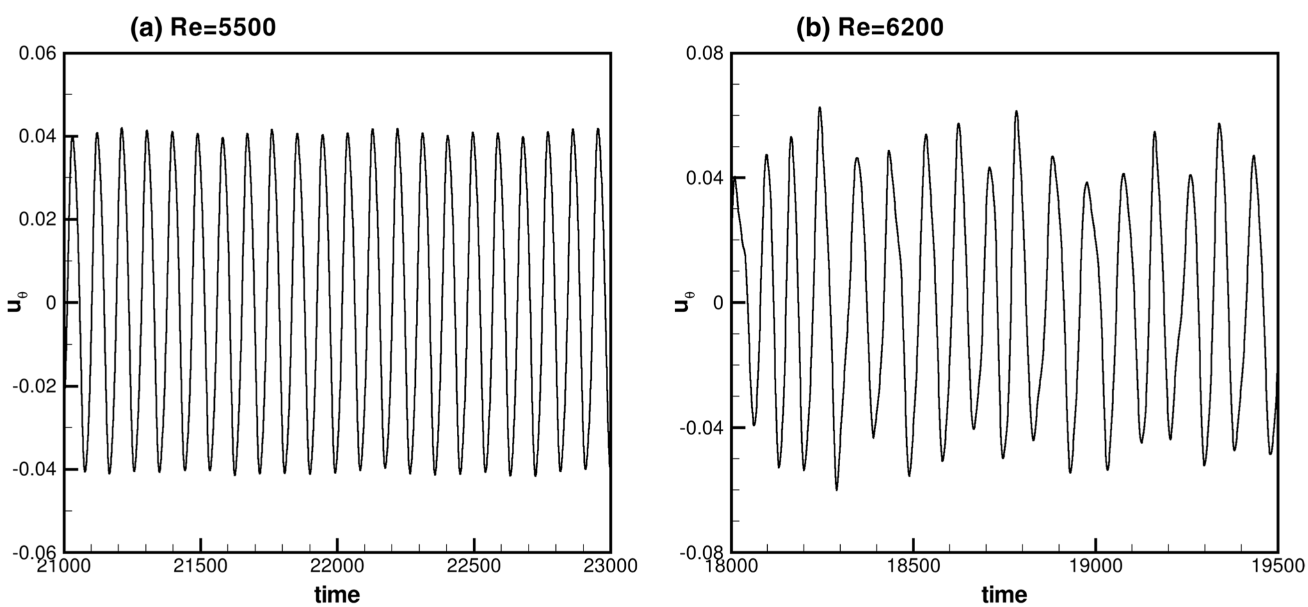

Fig. 13 Time history of the meridional velocity component u_θ of spiral wavy 1-vortex flow at a point $(r, \theta, \phi) = (1 + \beta/2, \pi/2, 0)$: **a** $Re = 5500$; **b** $Re = 6200$

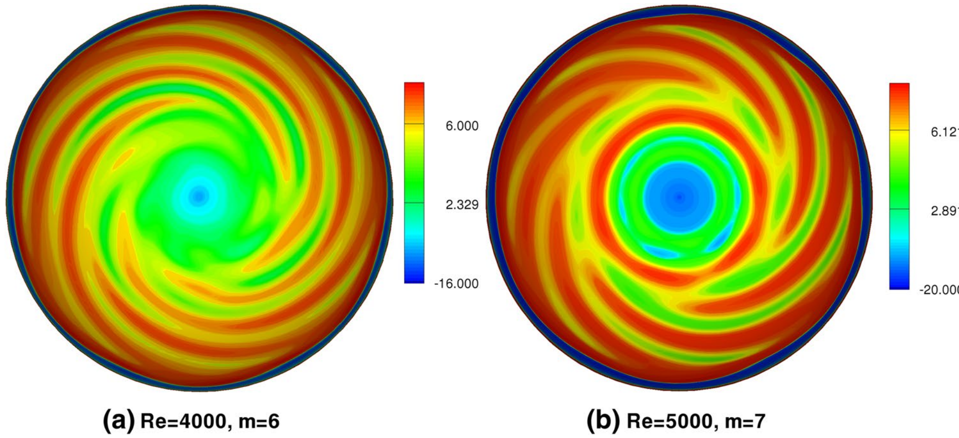

Fig. 14 North pole view of the colored contours of the azimuthal vorticity component ω_ϕ of spiral wavy 2-vortex flow at two different Reynolds numbers. The inner sphere rotates counterclockwise

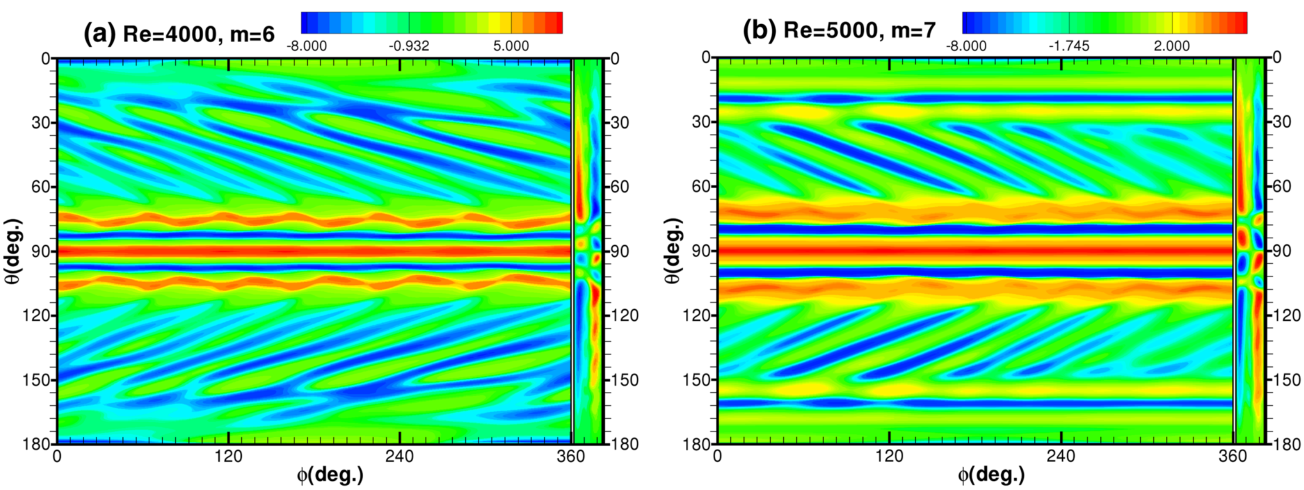

Fig. 15 Contours of the azimuthal angular velocity $\omega = v_\phi / r\sin(\theta)$ of the spiral wavy 2-vortex flow at two different Reynolds numbers on the middle spherical surface $r = 1 + 0.5\sigma$, $0 \le \theta \le \pi$, $0 \le \phi \le 2\pi$ on the left frame for each figure, while the right graph shows the streamlines in the meridional plane at $\phi = 2\pi$

$Re = 5000$ as the initial conditions and increasing the Reynolds number with the increments. Figure 11a shows the computed spiral wavy 1-vortex flow with spiral number $s_p = 3$ at $Re = 5500$. The spiral arms are clockwise from the high latitude to the equatorial regions. Figure 11b shows the three spiral waves remain but are distorted by counter-direction spreading spirals at $Re = 6000$. We see that for $Re > 6000$ the spiral flows become distorted and irregular flow structures occur.

Figure 12a, b shows the azimuthal angular velocity ($\omega = v_\phi / r\sin(\theta)$) in (θ, ϕ)-plane in spherical surface $r = 1 + 0.5\sigma$, $0 \le \theta \le \pi, 0 \le \phi \le 2\pi$ for the same flows in Fig. 11. It can be seen that the spiral waves have clockwise spirals from the high to low latitude regions. There are also small irregular spirals in the high latitude regions. The Taylor vortices keep $m = 7$ waveforms in the equatorial region.

Figure 13 shows the velocity-time series at a point $(r, \theta, \phi) = (1 + \beta/2, \pi/2, 0)$ for the spiral wavy 1-vortex at $Re = 5500$ and $Re = 6200$ respectively.

Third, to obtain the spiral waves for the 2-vortex flow, we increase the Reynolds number with an increment of $\Delta Re = 100$ from $Re = 2100$, where have obtained partially wavy 2-vortex flow. At $Re = 4000$ we obtain the spiral waves of wavenumber $m = 6$ in the middle latitudes. Further increasing Re, we obtain spiral waves of wavenumber $m = 7$ at $Re = 5000$. The colored contours of the spiral waves at $Re = 4000$ and $Re = 5000$ are shown in Figs. 14a, b respectively. These spiral waves are counterclockwise spirals when viewed from high to low latitude regions. *They are not reported in the literature*.

Figure 15 shows the azimuthal angular velocity ($\omega = v_\phi / r\sin(\theta)$) of spiral wavy 2-vortex flow in (θ, ϕ)-plane in spherical surface $r = 1 + 0.5\sigma$, $0 \le \theta \le \pi$, $0 \le \phi \le 2\pi$. The spiral waves are counterclockwise spirals spreading from high to low latitude regions. The direction is different from the clockwise direction for the cases of spiral 0- and 1-vortex flows. The boundaries between the outer and the

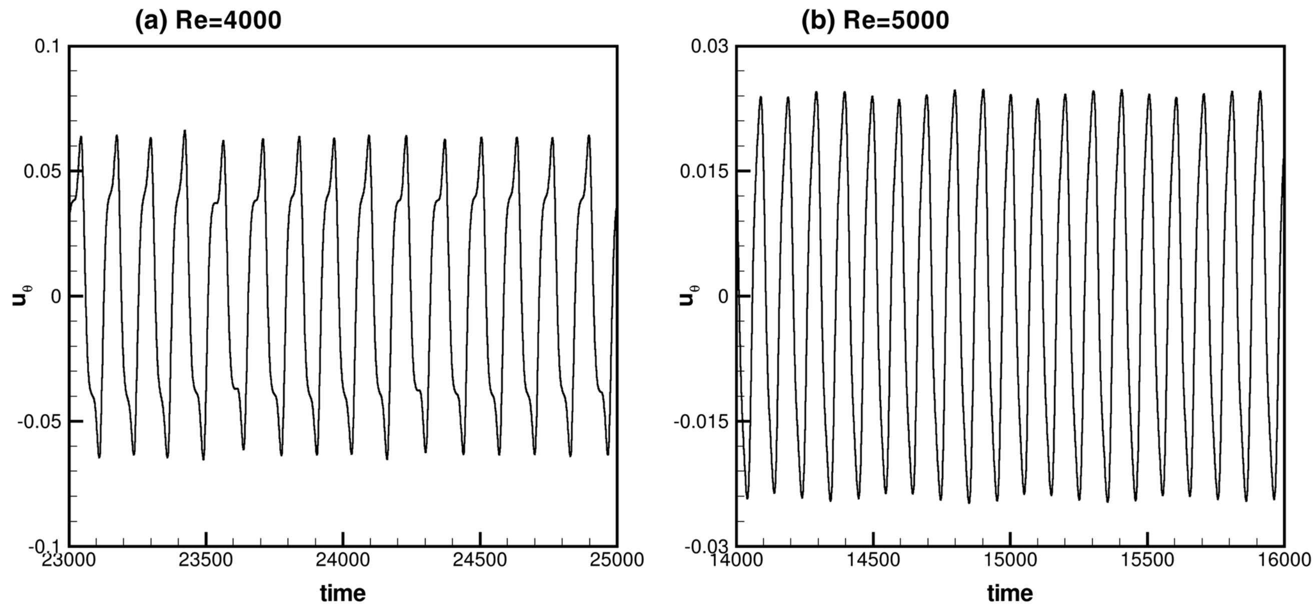

Fig. 16 Time history of the meridional velocity component u_θ of spiral wavy 2-vortex flow at a point $(r, \theta, \phi) = (1 + \beta/2, \pi/2, 0)$: **a** $Re = 4000$; **b** $Re = 5000$

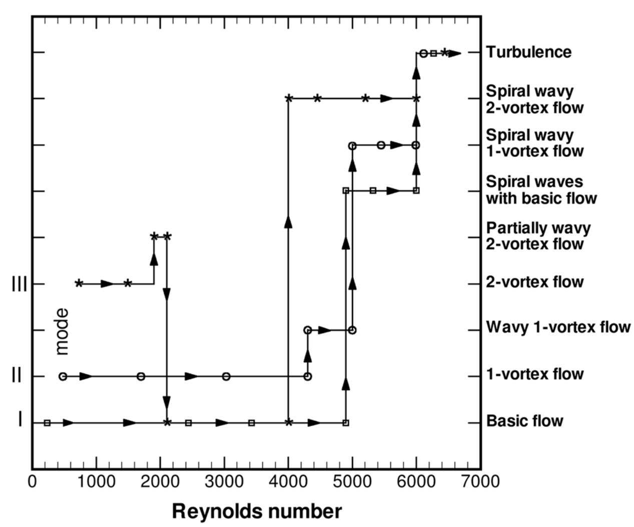

Fig. 17 Different flow modes and transitions in the clearance ratio $\sigma = 0.25$

inner vortices are wavy because of the influence of the spiral waves. The flow are not completely periodic as there are some non-periodic fluctuations in the high latitude and polar regions. When we further increase the Reynolds number above 6000 the flow evolves into turbulent 0-vortex flow.

Figure 16 shows the velocity-time series at a point $(r, \theta, \phi) = (1 + \beta/2, \pi/2, 0)$ for the spiral wavy 2-vortex at $Re = 4000$ and $Re = 5000$ respectively.

As a summary, Fig. 17 shows a sketch of the computed flow modes and transition paths with increasing Reynolds number for the clearance ratio $\sigma = 0.25$. This is a modified figure of figure 6 in [28] with some new spiral wavy disturbances. Figure 6 of [28] did not explain the flow modes after the wavy 2-vortex flow at $Re = 2000$, In present work, we have explained the flow pattern with the increasing Reynolds number. We have also simulated the flow modes at higher Reynolds number up to the turbulence for 0-, 1-, and 2-vortex flows, which is also missing in figure 6 of [28].

5 Conclusions

We have studied the multiple steady and unsteady flow modes in a medium-gap spherical Couette flow with only the inner sphere rotating and outer one fixed. An implicit line Gauss–Seidel scheme (LGS) has been used for numerical simulations of spherical Couette flow. This schemes is implemented along with a fifth-order finite difference WENO scheme in the artificial compressibility method.

By using these numerical schemes different flow modes for a medium-gap clearance ratio $\sigma = 0.25$ have been simulated in detail in the range $Re \in [400, 6500]$ with steps of $\Delta Re = 100$ and 10. It is found that steady 0-, 1-, and 2-vortex flows coexist in the range $700 \leq Re \leq 1900$. Wavy 1-vortex and 2-vortex flows are obtained in different narrow ranges of Reynolds numbers. With increasing Reynolds number, we obtain spiral waves of different wavenumbers for 0-, 1-, and 2-vortex flows at higher Reynolds numbers. The present critical Reynolds numbers for flow transitions are comparable to the existing experimental results. Further, we have first time simulated the spiral wavy 1-vortex flow, partially wavy 2-vortex flow and spiral wavy 2-vortex flow for this medium-gap clearance ratio.

Acknowledgements This work is supported by Natural Science Foundation of China (11321061, 11261160486, and 91641107) and Fundamental Research of Civil Aircraft (MJ-F-2012-04). Suhail Abbas thanks the financial support of CAS-TWAS President's Fellowship Program during his PhD study in University of Chinese Academy of Sciences, Beijing, China.

References

1. Harlow F, Welch J (1965) Numerical calculation of time-dependent viscous incompressible flow for fluid with free surface. Phys Fluids 8:21–82
2. Chorin A (1968) Numerical solution of the Navier–Stokes equations. Math Comput 22:745–762
3. Patanker S (1980) Numerical heat transfer and fluid flow. Hemisphere, Washington, DC
4. Van KJ (1986) A second-order accurate pressure-correction scheme for viscous incompressible flow. SIAM J Sci Stat Comput 7(3):870–891
5. Kim J, Moin P (1985) Application of a fractional time-step method to incompressible Navier–Stokes equations. J Comput Phys 59:308–323
6. Rosenfeld M, Kwak D, Vinokur M (1991) A fractional step solution method for the unsteady incompressible Navier–Stokes equations in generalized coordinate systems. J Comput Phys 94:102–137
7. Jordan SA (1996) An efficient fractional-step technique for unsteady incompressible flows using a semi-staggered grid strategy. J Comput Phys 127:218–225
8. Rogers S, Kwak D (1990) Upwind differencing scheme for the time-accurate incompressible Navier–Stokes equations. AIAA J 28(2):253–262
9. Rogers S, Kwak D, Kiris C (1991) Steady and unsteady solutions of the incompressible Navier–Stokes equations. AIAA J 29:603–610
10. Huang L (2000) Numerical solution of the unsteady incompressible Navier–Stokes equations on the curvilinear half-staggered mesh. J Comput Math 18(5):521–530
11. Briley W, Neerarambam S, Whitfield D (1996) Implicit lower–upper/approximate-factorization schemes for incompressible flows. J Comput Phys 128(1):32–42
12. Liu H, Kawachi K (1998) A numerical study of insect flight. J Comput Phys 146(1):124–156
13. Hartwich P, Hsu C (1987) High-resolution upwind schemes for the three-dimensional incompressible Navier–Stokes equations. AIAA paper 87–0547. AIAA Press, Washington, DC
14. Shah A, Yuan L (2011) Numerical solution of a phase-field model for incompressible two-phase flows based on artificial compressibility. Comput Fluids 42:54–61
15. Yang JY, Yang SC, Chen YN, Hsu CA (1998) Implicit weighted ENO schemes for three-dimensional incompressible Navier–Stokes equations. J Comput Phys 146:464–487
16. Bernardo C, Shu CW (1998) The Runge–Kutta discontinuous Galerkin method for conservation laws V: multidimensional systems. J Comput Phys 141:199–224
17. Kwak D, Chang J, Shanks S, Chakravarthy S (1986) A three-dimensional incompressible Navier–Stokes flow solver using primitive variables. AIAA J 24(3):390–396
18. Rogers S, Chang J, Kwak D (1987) A diagonal algorithm for the method of pseudocompressibility. J Comput Phys 73(2):364–379
19. Yoon S, Kwak D (1991) Three-dimensional incompressible Navier–Stokes solver using lower–upper symmetric-Gauss–Seidel algorithm. AIAA J 29(6):874–875
20. Rogers S (1995) Comparison of implicit schemes for the incompressible Navier–Stokes equations. AIAA J 33(11):2066–2072
21. Yuan L (2002) Comparison of implicit multigrid schemes for three-dimensional incompressible flows. Comput Phys 77:134–155
22. Nakabayashi K, Tsuchida Y, Zheng Z (2002) Characteristics of disturbances in the laminar-turbulent transition of spherical Couette flow, 1. Spiral Taylor–Görtler vortices and traveling waves for narrow gaps. Phys Fluids 14(11):3963–3972
23. Yavorskaya I, Belyaev Y, Monakhov A, Astaf N, Scherbakov S, Vvedenskaya N (1980) Stability, nonuniqueness and transition to turbulence in the flow between two rotating spheres. Report No. 595, Space Research Institute of the Academy of Science, USSR
24. Marcus P, Tuckerman L (1986) Simulation of flow between two concentric rotating spheres Part 1: Steady states. Fluid Mech 185:1–30 (**Simulations of flow between two concentric rotating spheres. Part 2: Transitions. ibid. 185:31–65**)
25. Yuan L, Fu DX, Ma YW (1996) Numerical study of bifurcation solutions of spherical Taylor–Couette flow. Sci China Ser A 39(2):187–196
26. Yuan L (2004) Numerical study of multiple periodic flow states in spherical Taylor-Couette flow. Sci China Ser A 47:81–91
27. Yuan L (2012) Numerical investigation of wavy and spiral Taylor–Gortler vortices in medium spherical gaps. Phys Fluids 24:104–124
28. Junk M, Egbers C (2000) Isothermal spherical Couette flow. In: Egbers C, Pfister G (eds) Physics of rotating fluids. Lecture notes in physics, vol 549. Springer, Berlin, pp 215–235
29. Sawatzki O, Zierep J (1970) Das Stromfeld im Spalt zwichen zwei konzentrischen Kulgelflachen, von denen die innere rotiert. Acta Mech 9:13–35
30. Munson B, Menguturk M (1975) Viscous incompressible flow between concentric rotating spheres. Part 3. Linear Stab J Fluid Mech 69:281–318
31. Wimmer M (1976) Experiments on a viscous fluid flow between concentric rotating spheres. J Fluid Mech 78:317–335
32. Bartels F (1982) Taylor vortices between two-concentric rotating spheres. J Fluid Mech 119:1–65
33. Nakabayashi K (1983) Transition of Taylor–Gortler vortex flow in spherical Couette flow. J Fluid Mech 132:209–230
34. Schrauf G (1986) The first instability in spherical Couette flow. J Fluid Mech 166:287–303
35. Nakabayashi K, Tsuchida Y (1995) Flow-history effect on higher modes in the spherical Coutte flow. J Fluid Mech 295:43–60
36. Shah A, Yuan L, Islam S (2012) Numerical solution of unsteady Navier–Stokes equations on curvilinear meshes. Comput Math Appl 63:1548–1556
37. Suhail A, Yuan L, Shah A (2018) Simulation of spiral instabilities in wide-gap spherical Couette flow. Fluid Dyn Res 50:025507
38. Suhail A, Yuan L, Shah A (2018) Existence regime of symmetric and asymmetric Taylor vortices in wide-gap spherical Couette flow. J Braz Soc Mech Sci Eng. 40:156
39. Liu M, Blohm C, Egbers C, Wulf P, Rath HJ (1996) Taylor vortices in wide spherical shells. Phys Rev Lett 77:286–289
40. Hollerbach R (1998) Time-dependent Taylor vortices in wide-gap spherical Couette flow. Phys Rev Lett 81:3132–3135
41. Hollerbach R, Junk M, Egbers C (2006) Non-axisymmetric instabilities in basic state spherical Couette flow. Fluid Dyn Res 38:257–273